

NUMERICAL MODELING FOR THE GASEOUS AND STELLAR STRUCTURE OF THE CENTRAL REGION OF NGC 4321

KEIICHI WADA

National Astronomical Observatory, Mitaka, Tokyo 181, Japan; wada@th.nao.ac.jp

KAZUSHI SAKAMOTO

Caltech, Radio Astronomy Department, 105-24, Pasadena, CA 91125; ks@astro.caltech.edu

AND

TAKEO MINEZAKI¹

National Astronomical Observatory, Osawa 2-21-1, Mitaka, Tokyo, 181, Japan; minezaki@asterope.mtk.nao.ac.jp

Received 1997 April 18; accepted 1997 August 29

ABSTRACT

Hydrodynamic simulations have been compared with high-resolution CO ($J = 1-0$) observations of the central region ($R < 1.5$ kpc) of NGC 4321. In the simulations, the evolution of a self-gravitating gas disk in gravitational potentials that suitably match the nuclear bar of NGC 4321 has been followed. Postulating that the nuclear bar of $R \sim 16''$ governs nearby gas dynamics, we determine a set of parameters to reproduce the observed gas structure, which includes two trailing spirals and a dense nuclear concentration. The pattern speed of the nuclear bar is $65 \text{ km s}^{-1} \text{ kpc}^{-1}$, and the total gas mass in the central region is $\sim 1.0-1.3 (T_g/10^4 \text{ K})^{1/2} \times 10^9 M_\odot$, where T_g is the gas kinematic temperature. In addition, the observed molecular spirals have been found to be short-lived but recurrent. It has been found that the observed gas features cannot be reproduced from the gravitational potential derived from a K' -band image if a constant mass-to-luminosity ratio is assumed. From the K' -band image and the gravitational potential of the best-fit analytical model, a two-dimensional map of the mass-to- K luminosity ratio (M/L_K) has been obtained. This ratio ranges from 0.2 to 1.2 (M/L) $_\odot$ in the central region; the smallest value occurs at star-forming regions located at each end of the nuclear bar. Our numerical approach is an effective way to estimate the mass distribution and the pattern speed in spiral galaxies.

Subject headings: galaxies: individual (NGC 4321) — galaxies: ISM —
 galaxies: kinematics and dynamics — galaxies: spiral — hydrodynamics —
 methods: numerical

1. INTRODUCTION

Numerical modeling of the interstellar gas in galaxies is an effective approach to infer galactic gravitational structure. This is because the dynamical behavior of gas is very sensitive to the background gravitational potential. For example, gas tends to form spiral, ring, or barlike structures in a nonaxisymmetric potential, even if its distortion is very weak (Wada & Habe 1995, and references therein). These structures, which are often seen in the central regions of spiral galaxies, are related to dynamical resonances (inner Lindblad resonances [ILRs] in particular). Since the dynamical resonances depend closely on the mass distribution and the pattern speed of the nonaxisymmetric component (hereafter referred to as the “bar”), it is possible to determine these dynamical parameters by comparison of numerical simulations and gas observations.

Our previous paper (Sakamoto et al. 1995, hereafter Paper I) concerned the stellar and gaseous structure in the central few kiloparsecs of NGC 4321. It was determined that most of the molecular gas is distributed in a central dense core and in two-armed spirals emanating at the ends of a nuclear stellar bar (of $R \sim 16'' \sim 1.3$ kpc) found by the observations in the near-infrared (Knapen et al. 1995a; Shaw et al. 1995; Paper I). It was qualitatively explained in Paper I that the molecular spiral structure seen in the CO map was due to the outer ILR and that the compact molec-

ular core at the galactic center was formed through gravitational instability at the inner ILR. With these conspicuous nuclear gas structures, NGC 4321 is undoubtedly among the best targets for detailed numerical modeling. The present paper is aimed at confirming quantitatively the ILR model reported in Paper I and comparing numerical simulations with the CO observations to determine important dynamical parameters. The parameters to be determined include the pattern speed of the bar, the gas mass, and mass distribution.

There have been two numerical simulations of the gaseous and stellar structure of NGC 4321. Knapen et al. (1995a), using high-resolution NIR imaging and three-dimensional numerical modeling of stellar and gas dynamics, reproduced a two-armed gaseous spiral structure similar to the observed spirals in an “NGC 4321-like” N -body bar. Although they found that either nuclear leading spirals or an oval ring is formed inside the trailing spirals, the dense nuclear core observed by CO was not reproduced. Their three-dimensional N -body bar model is more realistic than our model, i.e., a two-dimensional rigid bar potential. However, the N -body bar is not favorable for control of the dynamical parameters, such as the strength and the pattern speed of the bar, and therefore it is not easy to examine the parameter dependence of the gaseous structure. Meanwhile Sempere et al. (1995) concluded that the pattern speed of the outer bar (of $R \sim 60'' \sim 5$ kpc) is $20 \text{ km s}^{-1} \text{ kpc}^{-1}$ and that the ILRs are located at $R = 0.4$ and 2.5 kpc. The difference between the present study and that of Sempere et al. is that their simulations are mainly con-

¹ Current address: Kiso Observatory, Institute of Astronomy, Faculty of Science, University of Tokyo, Mitake-mura, Kiso-gun, Nagano 397-01, Japan; minezaki@kiso.mtk.ioa.s.u-tokyo.ac.jp.

cerned with observations of the outer regions of NGC 4321, while this study concentrates on the nuclear regions.

In § 2, the gravitational potential models, gas disk models, and the numerical method are described. In § 3, the numerical results are compared with the observations, and the best-fit model is determined. In § 4, the determined pattern speed of the bar, mass distribution, and gas mass are discussed. Conclusions are summarized in § 5.

2. NUMERICAL MODELS AND METHOD

2.1. Potential Models

Two sets of potential models were used to simulate gas dynamics in NGC 4321. The first is a set of potential models of an analytical bar, and the second is a set of potential models derived from the near-infrared light distribution of NGC 4321, assuming a constant mass-to-luminosity ratio (“NIR models”). Both models were two-dimensional; the vertical structure was not taken into account in the simulations. It was also assumed that the gravitational potential did not depend on time, that the gaseous evolution did not affect the potential, and that the nonaxisymmetric part of the potential rotated rigidly at an angular velocity Ω_p .

2.1.1. Analytical Bar Models

It is postulated that the gaseous dynamics in the nuclear region of NGC 4321 are governed by the nuclear bar ($R \sim 1.3$ kpc) rotating at Ω_p . The justification of this postulation is the fact that the gravitational torque exerted on the central gas due to the nuclear bar is much larger than that due to the outer bar. The contribution of the outer bar on the potential in the nuclear bar region is less than a few percent. The relations between the nuclear bar and the outer bar are discussed in § 4.1.

The potential of the analytical models is

$$\Phi(R, \phi) = \Phi_0(R) + \Phi_1(R, \phi), \quad (1)$$

where Φ_0 and Φ_1 are axisymmetric and nonaxisymmetric potentials, respectively. We use the “Toomre disk” potential (Toomre 1963) for the axisymmetric part. The potential has two parameters, a (scale parameter called “core radius”) and v_{\max} (the maximum rotation speed), and is expressed as

$$\Phi_0(R) = \frac{c^2}{a} \frac{1}{(R^2 + a^2)^{1/2}}, \quad (2)$$

where c is given as $c \equiv v_{\max}(27/4)^{1/4}a$. We also added, to some models, an “extended disk” component that has the same form as equation (2) with a core radius of 10 kpc and v_{\max} of 200 km s^{-1} . The nonaxisymmetric part of the potential is assumed to be of the form

$$\Phi_1(R, \phi, t) = \epsilon(R)\Phi_0 \cos 2(\phi - \Omega_p t), \quad (3)$$

where $\epsilon(R)$ is given as

$$\epsilon(R) = \epsilon_0 \frac{aR^2}{(R^2 + a^2)^{3/2}}. \quad (4)$$

The parameter ϵ_0 represents the strength of the bar, and Ω_p denotes the pattern speed of the bar. This formalism is taken from Sanders (1977). The parameter ϵ_0 is at full strength from the beginning of simulations. Since our bar

models are weak ($\epsilon_0 = 0.03\text{--}0.12$), initial strong shocks and subsequent accretion of gas to the galactic center do not occur.

2.1.2. NIR Models

The NIR potential models are derived from a near-infrared image of NGC 4321, assuming that the mass-to-luminosity ratio (M/L_K) is constant in a calculating region, which is the central 8×8 kpc. It is assumed that the nuclear and outer bars rotate at a single pattern speed Ω_p ; i.e., they actually are a single bar. The NIR imaging procedure was described in Paper I. We use here a slightly better image (i.e., $2''.5$ seeing) taken after the one reported in Paper I. The gravitational potential $\Phi_{\text{NIR}}(i, j)$ at a mesh point (i, j) is derived as

$$\Phi_{\text{NIR}}(i, j) = \alpha \sum_{i', j'} \mathcal{G}_{i-i', j-j'} \mu_{i', j'}, \quad (5)$$

where α is a constant defined as $M/L_K = \alpha(M/L)_\odot$, \mathcal{G} is the Green’s function of point mass gravity, and $\mu_{i', j'}$ is the K' surface luminosity at a mesh point (i', j') . With the convolution theorem, the local potential is written as $\hat{\phi}_{i, j} = \hat{\mathcal{G}}_{i, j} \hat{\mu}_{i, j}$, where the circumflex denotes the coefficient of the Fourier transform (Hockney & Eastwood 1981, p. 211). The total number of the grid cells for fast Fourier transform (FFT) are 512×512 . We use 105×105 pixels ($\sim 8 \times 8$ kpc) of a central region in the K' image, and they are assigned to the 256×256 FFT grid cells.

2.2. Gas Disk Models

The two potential models were applied to a common gas disk model. In these models, the gas is treated as a compressive self-gravitating fluid, and the smoothed particle hydrodynamics (SPH) method is used to calculate the hydrodynamic evolution of the gas disk. Initially, 10,000 SPH particles are randomly distributed in a disk of 1.5 kpc. An initial rotational velocity is given in order to balance a radial component of the gravitational force. Star formation is ignored, and an isothermal gas of temperature T_g ($T_g = 2500\text{--}40,000$ K) is assumed. The gas “temperature” here is not the thermal temperature of the molecular gas but the kinematic temperature of the gas cloud system. The initial gas disk with $T_g > 10^4$ K is gravitationally stable. The Toomre Q -value is 1.7 at $R = 1.5$ kpc and 3.3 at $R = 1.0$ kpc.

Parameters of the analytical bar models and the gas disks are summarized in Tables 1 and 2.

2.3. Numerical Method

The equations of motion of the i th SPH particles on the rotating coordinate of the bar potential are

$$\frac{d\mathbf{r}_i}{dt} = \mathbf{v}_i, \quad (6)$$

$$\begin{aligned} \frac{d\mathbf{v}_i}{dt} = & -\nabla\Phi - \nabla\Phi_g - \frac{1}{\rho_i} \nabla(P_i + q_i) \\ & + 2(\boldsymbol{\Omega}_i \times \mathbf{v}_i) + \boldsymbol{\Omega}_p \times (\boldsymbol{\Omega}_p \times \mathbf{r}_i), \end{aligned} \quad (7)$$

where $\Phi \equiv \Phi_0(R) + \Phi_1(R, \phi)$ for the analytical bar model and $\Phi \equiv \Phi_{\text{NIR}}(x, y)$ (eq. [5]) for the NIR model. The posi-

TABLE 1
PARAMETERS OF THE ANALYTICAL BAR MODELS

Model	Ω_p (km s ⁻¹ kpc ⁻¹)	a (kpc)	v_{\max} (km s ⁻¹)	M_g (10 ⁹ M_\odot)
1	100	2.0	200	0.1
2	70	0.7	200	0.2
3	70	0.5	200	0.2
4	70	0.4	180	0.5
5	65	0.4	180	0.5
6	60	0.5	200	0.2
7	60	0.4	180	1.0
8	60	0.4	180	0.5
9	60	0.3	180	0.5
10	50	2.0	200	0.1
11	50	1.0	200	0.1
12	50	0.7	200	0.2
13	50	0.5	200	0.5
14	50	0.5	200	0.2
15	50	0.4	200	0.2
16	50	0.4	180	0.2
17	50	0.4	160	0.5
18	30	1.0	200	0.1
19	30	0.7	200	0.2
20	30	0.5	200	0.2

NOTE.—The gas kinematic temperature $T_g = 10^4$ K and $\epsilon_0 = 0.05$ (eq. [4]) are used in all models.

tions from the center of the disk and velocity vector of the i th particle are r_i and v_i , respectively, and P_i and q_i are the gas pressure and the artificial viscosity, respectively. The SPH code used here is based on Wada & Habe (1992, 1995).

TABLE 2
PARAMETERS OF THE ANALYTICAL BAR MODELS

Model	Ω_p (km s ⁻¹ kpc ⁻¹)	ϵ_0	M_g (10 ⁹ M_\odot)	T_g (10 ⁴ K)
21	80	0.07	1.0	1.0
22	70	0.07	1.0	1.0
23	65	0.15	2.0	4.0
24	65	0.12	1.0	1.0
25	65	0.10	2.0	4.0
26	65	0.07	3.0	4.0
27	65	0.07	2.5	4.0
28	65	0.07	2.0	4.0
29	65	0.07	1.5	4.0
30	65	0.07	1.0	4.0
31	65	0.07	1.0	1.0
32	65	0.07	1.0	0.25
33	65	0.07	0.5	4.0
34	65	0.05	2.0	4.0
35	65	0.05	2.0	4.0
36	65	0.05	1.0	1.0
37	65	0.04	1.0	1.0
38	65	0.03	2.0	4.0
39	60	0.10	1.0	1.0
40	60	0.07	1.5	1.0
41	60	0.07	1.0	1.0
42	60	0.07	0.5	1.0
43	60	0.07	1.5	4.0
44	60	0.07	1.0	4.0
45	60	0.05	1.0	1.0
46	55	0.07	1.0	1.0
47	50	0.07	2.5	4.0
48	50	0.07	2.0	4.0
49	50	0.07	1.5	4.0
50	50	0.07	1.0	1.0
51	40	0.07	2.5	4.0
52	40	0.07	2.0	4.0
53	40	0.07	1.0	1.0

NOTE.—The core radius of the potential $a = 0.3$ kpc and the maximum rotational velocity $v_{\max} = 180$ km s⁻¹.

We use the Gaussian kernel

$$W(|r_i - r_j|) \equiv \frac{1}{\pi^{3/2} h_i^3} \exp\left(-\frac{|r_i - r_j|^2}{h_i^2}\right), \quad (8)$$

where m is the mass of a particle and the particle “size” h_i is varied depending on the local gas density as $h_i \propto \rho_i^{-1/3}$. The artificial viscosity q_i in equation (7) is given by

$$\frac{1}{\rho_i} \nabla q_i = \sum_j \left(\frac{P_i}{\rho_i^2} + \frac{P_j}{\rho_j^2} \right) (-\alpha \mu_{ij} + \beta \mu_{ij}^2) \nabla W(|r_i - r_j|), \quad (9)$$

$$\mu_{ij} \equiv \frac{2h_i v_{ij} \cdot r_{ij}}{c_s(r_{ij}^2 + 0.1h_i^2)}, \quad \alpha = 0.5, \beta = 1.0, \quad (10)$$

where c_s is the sound velocity and α and β are chosen to represent a shock wave.

Self-gravitational potential of the gas, Φ_g , is calculated from the gas distribution using the procedure described in § 2.1.2. The size of grid cells is 36 pc. The equations of motion (eqs. [6] and [7]) are integrated using the standard leapfrog algorithm.

The units of time, distance, mass, and rotational frequency are $T = 10^6$ yr, $L =$ kpc, $M = 10^9 M_\odot$, and $\Omega =$ km s⁻¹ kpc⁻¹, unless otherwise noted.

3. RESULTS

The numerical results of the two potential models were compared with the CO observations reported in Paper I. The main results of the observations were as follows (see also Fig. 1 [Pl. 7]): (1) The total molecular gas mass in the central 3 kpc is $M_{\text{H}_2+\text{He}} = 2.2 \times 10^9 M_\odot$. (2) There are two-armed spiral features of molecular gas starting at the rims of the nuclear bar. Several gas clumps are on the arms. (3) There is a central CO concentration of ~ 250 pc diameter and $2.6 \times 10^8 M_\odot$ of gas mass. (4) The velocity field shows noncircular motions, which are especially large at the spiral arms. Note that the masses above are estimated using the Galactic CO-to-H₂ conversion factor [$X = 3 \times 10^{20}$ cm⁻² (K km⁻¹ s⁻¹)⁻¹].

3.1. Analytical Bar Model

3.1.1. The Best-Fit Model

By comparing the observed integrated intensity map, the isovelocity map, and the position-velocity map with the numerical one, the pattern speed of the bar, the mass distribution, and the total gas mass have been successfully determined. Figure 2 shows the evolution of an analytical bar model (model 31), which was compared with the CO integrated intensity map and the position-velocity (P-V) diagram along the major axis (P.A. = 155°). A snapshot ($T = 101.67$ Myr) shows the best match to the observations in this model. As seen in the CO integrated intensity map, the two-armed trailing spirals and the central concentration are reproduced, and there are also several density peaks on the two trailing spirals. The P-V diagram also agrees well with the observations. After many trials with a wide range of parameters (Tables 1 and 2), it was determined that model 31 is the best-fit model. Its parameters are $\Omega_p = 65$ km s⁻¹ kpc⁻¹, $M_g = 1.0 \times 10^9 M_\odot$, $a = 300$ pc (eq. [2]), $v_{\max} = 180$ km s⁻¹ (eq. [2]), $\epsilon_0 = 0.07$ (eq. [4]), and $T_g = 1.0 \times 10^4$ K. In Figure 3, $\Omega(R)$ and $\Omega(R) - \kappa(R)/2$ diagrams are drawn, where $\Omega(R)^2 \equiv -d\Phi(R_0)/dR$ and

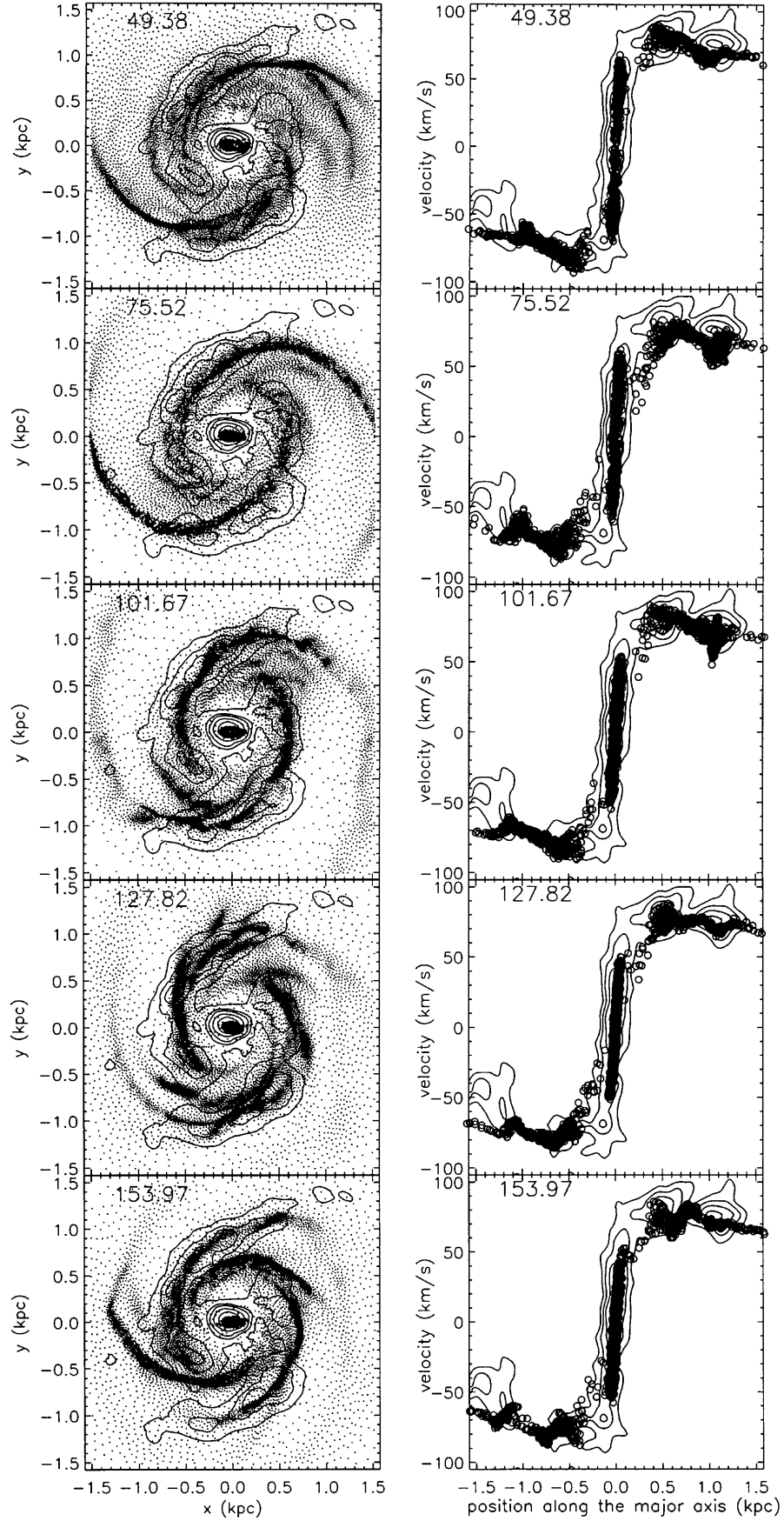


FIG. 2.—Time evolution of the best-fit analytical bar model (model 31). Contours in the left column are the CO integrated intensity map, and those in the right column are the P-V map along the major axis (Paper I). The models and observations are corrected in a face-on view. Unit of time is 10^6 yr. The rotating period of the bar is $T_{\text{bar}} = 2\pi/\Omega_p = 95 \times 10^6$ yr.

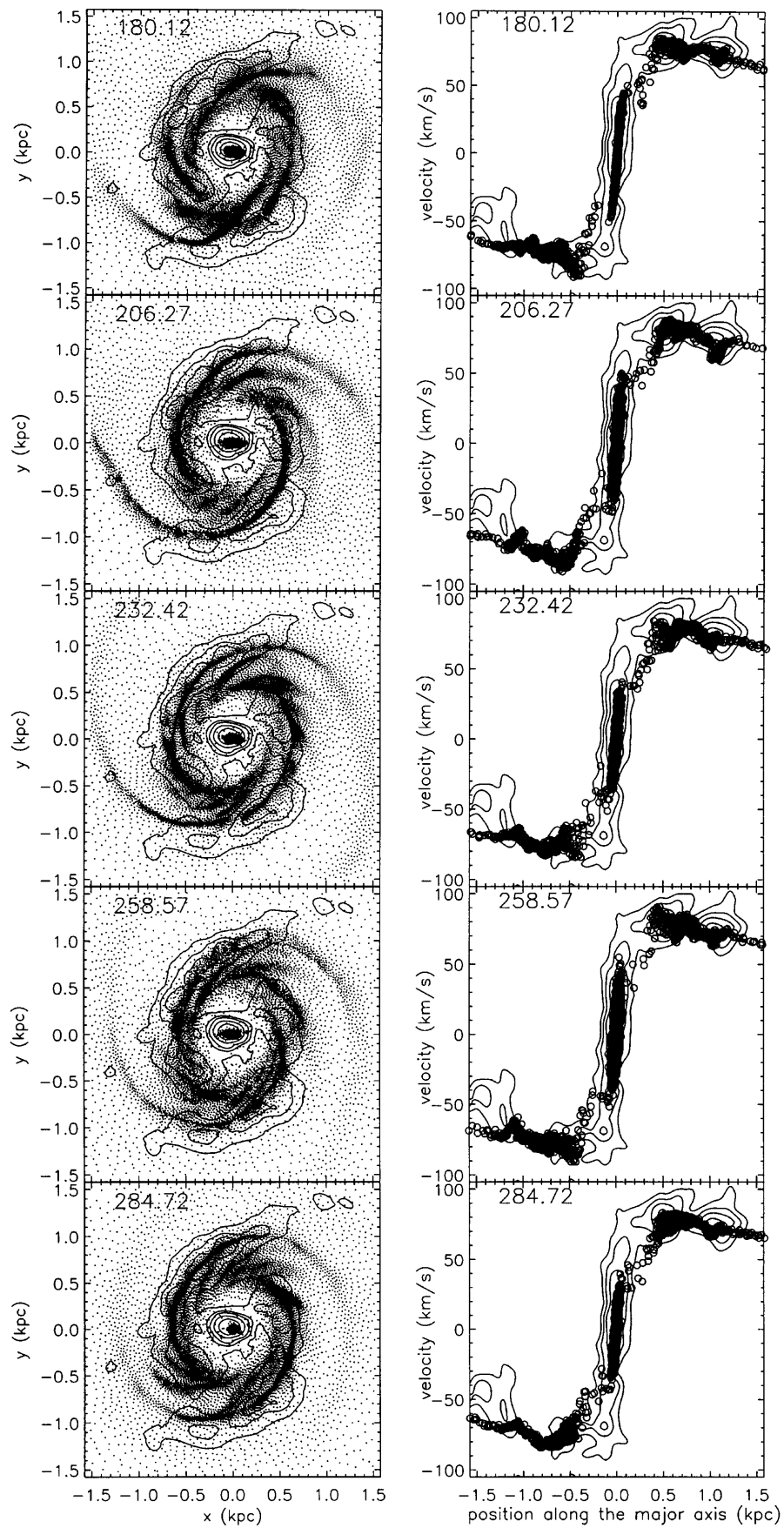


FIG. 2—Continued

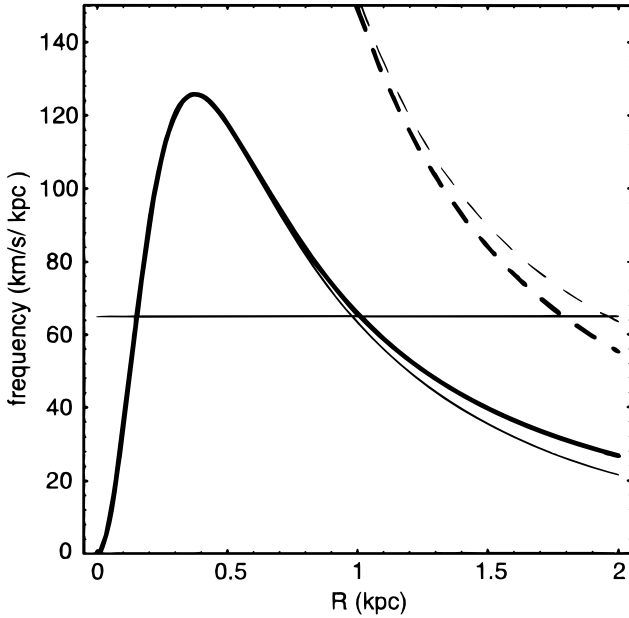


FIG. 3.— $\Omega(R)$ (dashed curves) and $\Omega(R) - \kappa(R)/2$ (solid curves) diagrams for the axisymmetric part of the potential of the best-fit model 31. Thin curves are drawn for the potential with the extended disk potential (a core radius of 10 kpc and $v_{\max} = 200 \text{ km s}^{-1}$). A thin horizontal line is the pattern speed of the best-fit model 31.

$\kappa(R)^2 \equiv 4\Omega(R)^2 + R d\Omega(R)^2/dR$. The inner ILR, outer ILR, and the corotation are located at $R \sim 0.2, 1.0, 1.9$ kpc, respectively, for $\Omega_p = 65 \text{ km s}^{-1} \text{ kpc}^{-1}$.

The gas evolution was not significantly affected when we added an axisymmetric potential with a core radius of 10 kpc and $v_{\max} = 200 \text{ km s}^{-1}$ that is regarded as an extended disk component. This is reasonable because the $\Omega - \kappa/2$ diagram is not much different from the model with the extended disk component (the thin lines in Fig. 3). Thus the parameters of model 31 are the best for reproduction of the observations regardless of whether the extended disk component is added. We have also found that the gaseous distribution is not steady; the spiral arms change their morphology in about 10^7 yr, and they appear at the observed position every about $(8-10) \times 10^7$ yr. This suggests that the observed molecular spirals are short-lived and recurrent. The gas distribution after a long period of evolution ($t \sim 700 \sim 8$ bar rotations) is similar to that in the early stages ($t < 300$), although it is somewhat smoother. Only the gas located inside $R \sim 500$ initially falls and forms the nuclear concentration. This nuclear inflow could cause the nuclear star-forming activity observed by H α (Cepa & Beckman 1990).

Using the Gaussian beam of FWHM 200 pc, we generate a “convolved” density map and an isovelocity contour map from the best-fit snapshot of model 31 (Fig. 4 [Pl. 8]). Comparing these maps with Figure 1, the agreement between the models and the observations is clear, especially in highly dense regions. Distortion of the velocity field at the spiral arms is well-reproduced. Positions of clumps on the arms in the numerical models do not completely agree with the observations, but this is reasonable if the clumps are formed by the gravitational instability on the arms. Actually, Toomre’s stability parameter Q implies that the clumps are formed through the local gravitational instability: $Q = 0.8$ and $\lambda_{\text{crit}} \equiv 2\pi G \Sigma_{\text{gas}} / \kappa^2 \sim 100 \text{ pc}$ at $R = 1.0$ for $\Sigma_{\text{gas}} = 500 M_{\odot} \text{ pc}^{-2}$.

The gas distribution and the velocity field do not fit the observations in relatively low-density regions, such as the outer part of the arms, and the region between the arms and the central core. The outer part of the northern arm in the model winds more tightly than observed in NGC 4321. The two observed arms are not symmetric about the center. This is probably a secondary effect of the nonaxisymmetric potential of the outer bar and distortion of the potential of $m \neq 2$ mode, because the near-infrared image of the outer bar region does not show complete bisymmetry.

3.1.2. Pattern Speed, Shape, and Mass of the Nuclear Bar

In order to establish the uniqueness of the best-fit model, results of models with parameters near those of the best-fit model are presented. As seen in Figure 5, the trailing spiral arms are formed outside the observed CO arms for the slower bar (model 50: $\Omega_p = 50$), if other parameters are the same as for the best-fit model. On the contrary, the spiral arms are formed inside the CO arms for the faster bar (model 22: $\Omega_p = 70$), and an oval gas ring appears in the center (Fig. 5, *bottom*). From these results, we conclude that the pattern speed of the bar should be in the range of $50 < \Omega_p < 70 \text{ km s}^{-1} \text{ kpc}^{-1}$. The presence of two ILR’s in this region, which is expected from the $\Omega - \kappa/2$ diagram (Fig. 3), is confirmed by the dependence of the locations of the spiral arms and the nuclear ring size on the pattern speed. Consequently, the conclusion of Paper I is quantitatively confirmed: the trailing spirals are driven by the outer ILR, and the nuclear core is debris of the leading spirals caused by the inner ILR.

The shape and the depth of the gravitational potential are parameterized by the core radius a , the maximum circular velocity v_{\max} , and the bar strength ϵ_0 (see eqs. [2] and [4]). The core radius was swept between 2.0 and 0.3 kpc (models 1–20), and the best-fit value was found to be 0.3 kpc. The larger cores were rejected because they produce a large nuclear ring at the inner ILR, which would have been resolved by our observations.

Since the P-V diagrams, especially at the flat rotation locations, depend on the depth of the potential, v_{\max} can be determined from a comparison between the observed P-V diagram and the numerical one. We have tested $v_{\max} = 150-200 \text{ km s}^{-1}$ and have found that 180 km s^{-1} is most likely. To determine the bar strength, i.e., the degree of the distortion, we have varied ϵ_0 from 0.03 to 0.15 for $\Omega_p = 60-65$. For a very weak bar (model 37: $\epsilon_0 = 0.04$), it is found that the spirals are vaguer than those in the best-fit model, and that a nuclear ring of about 200 pc radius is formed (Fig. 6, *top*). The nuclear ring is also seen as the two separated components at the rigid-rotation part of the P-V diagram. In contrast, a very compact core with small velocity dispersion is formed for a stronger bar (model 24: $\epsilon_0 = 0.12$) (Fig. 6, *bottom*). These results show that the observations are reproduced by neither a strong bar nor a weak bar. We therefore conclude that ϵ_0 must be 0.05–0.10, and $\epsilon = 0.07$ is the most probable value.

The above conclusion, i.e., model 31 is the best-fit model, is quantitatively reinforced by calculating the total root mean square residual between models and the observations with respect to the surface density and velocity field (Table 3). The residual for the surface density is an indicator of morphological coincidence between models and observations, and it is the minimum for the best-fit model 31. Although the residual for the arm regions of model 24 (a

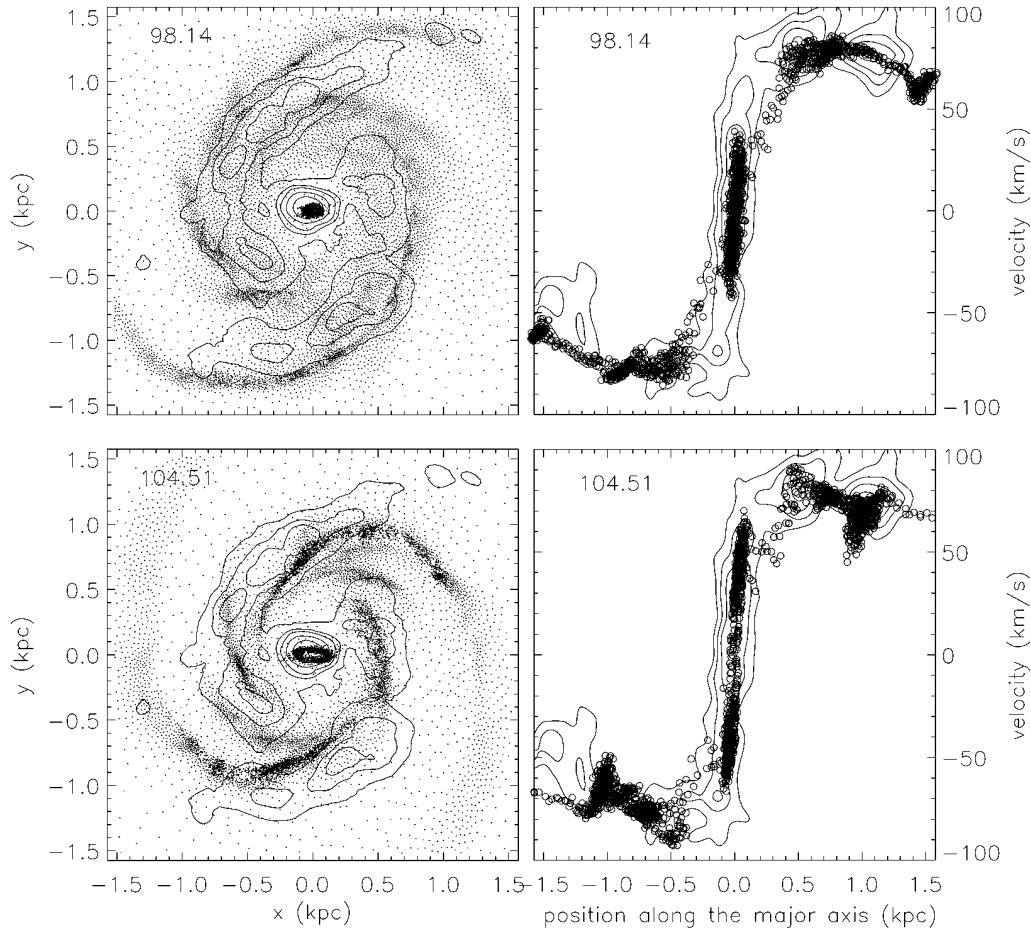


FIG. 5.—Same as Fig. 2, but for model 50 (top) and model 22 (bottom)

strong bar) is about 6% smaller than that of model 31, the residual for the core region is larger than that of the best-fit model by about factor of 3. It has been found that the rms residual for the velocity fields does not tightly depend on the parameters, such as the bar strength and the pattern speed of the bar. In other words, we cannot use the velocity fields to search for the best parameters in models whose P-V diagrams do not substantially differ from the observed one. For example, the P-V diagrams along the major axis look nearly the same for the models shown in Figures 2, 5, and 6.

TABLE 3
COMPARISON BETWEEN MODELS AND OBSERVATIONS

MODEL	DENSITY ^a		VELOCITY ^b	
	Core ^c	Arm ^d	Core	Arm
31 (Figure 4)	1.00	1.00	19.0	13.8
22 (Figure 5)	1.03	1.22	15.5	13.0
50 (Figure 5)	1.22	1.18	19.1	15.0
24 (Figure 6)	2.85	0.94	22.5	17.6
37 (Figure 6)	1.43	1.07	15.6	12.7
NIR (Figure 8)	9.06	1.48	27.7	19.4

^a Total root mean square residual between CO integrated intensity (Fig. 2) and convolved surface density of models. Normalized for model 31.

^b Total root mean square residual (km s⁻¹) between the line-of-sight velocity of the observations and models.

^c For the central region ($R < 200$ pc).

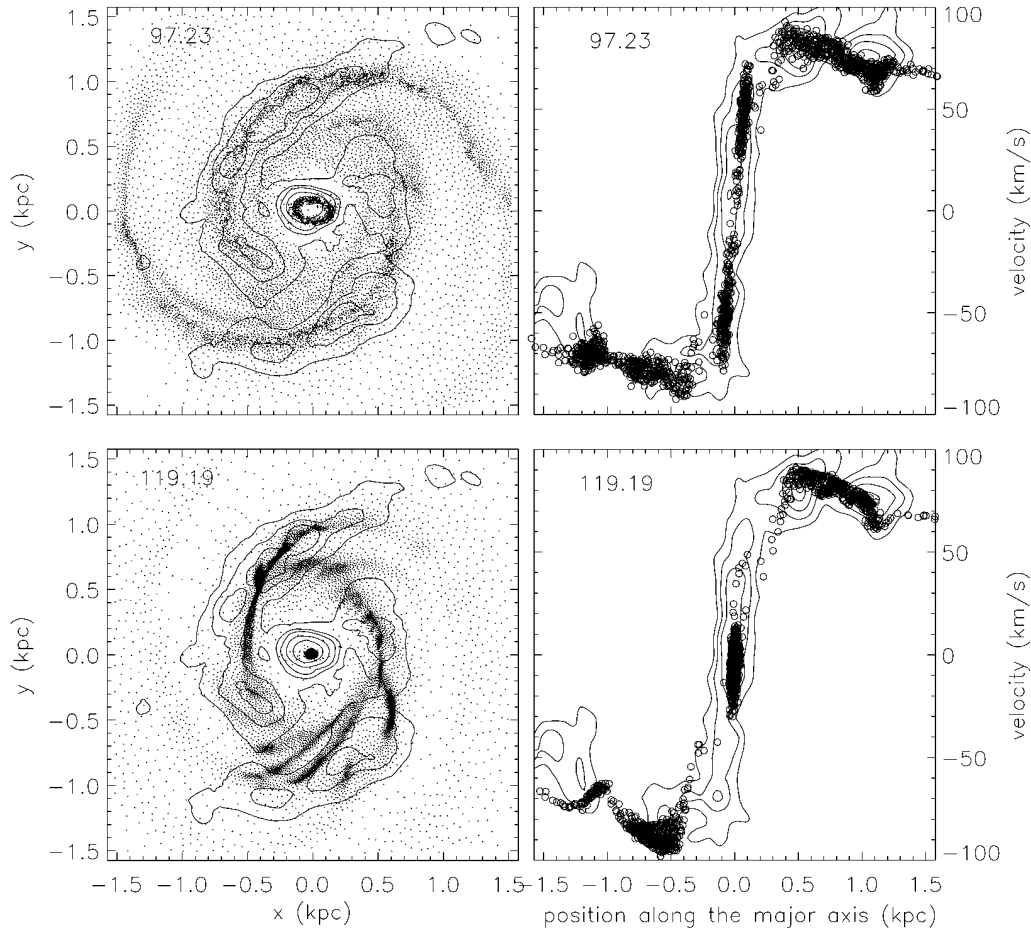
^d For regions of the spiral arms ($R > 200$ pc).

Moreover, one should notice that the P-V diagrams in Figure 2 do not depend on the gaseous morphology.

3.1.3. Gas Mass

The gaseous morphology also depends on the total gas mass M_g . In a less massive disk ($M_g = 0.5 \times 10^9 M_\odot$: model 42), trailing spiral arms are formed, but prominent gas clumps as seen in CO are not formed on the arms. This is in contrast to a more massive disk ($M_g = 1.5$: model 40), where many small spiral-like arms are formed through gravitational instabilities and then collapse into clumps (Fig. 7). The disk is unstable from the beginning ($Q = 0.8$ for $R = 1.5$ at $t = 0$). As a result, the two-armed trailing spirals observed by CO do not appear in the massive disk. The gas mass may thus be constrained in this way.

For a higher or lower kinematic temperature, the gas should be more or less massive to reproduce the observations. In other words, the total gas mass estimated from the simulations depends on the gaseous kinematic temperature. If $\Omega_p = 65$ and $T_g = 4 \times 10^4$ K, the trailing spirals do not form at the observed position for $M_g = 0.5$ (model 33) and 1.0 (model 30). The models with $M_g = 1.5, 2.0$, and 2.5 (models 29, 28, and 27, respectively) show results similar to the observations. Among these three models, model 28 shows the best fit. A more massive disk with $M_g = 3.0$ (model 26) does not reproduce the observations for both the two-dimensional distribution and the P-V diagram. On the other hand, a very low temperature model with $T_g = 2500$ K and $M_g = 1.0$ (model 32) is gravitationally unstable, and

FIG. 6.—Same as Fig. 5, but for model 37 (*top*) and model 24 (*bottom*)

the disk fragments to several clumps as seen in model 40. These results and the best-fit model suggest that the total gas mass in the region of $R < 1.5$ kpc of NGC 4321 is $\sim 1.0\text{--}1.3 \times 10^9 (T_g/10^4 \text{ K})^{1/2} M_\odot$. Although the temperature dependence (i.e., $T_g^{1/2}$) is a rough approximation, it is consistent with the criterion for the local gravitational instability.

3.2. NIR Models and M/L Distribution

Figure 8 shows one result from the NIR model; the set of best parameters for the analytical model and a mass-to-luminosity ratio $\alpha = 0.4$ are used. Obviously, the numerical result and the observations do not match, except at the dense central core. No model that reproduces the CO

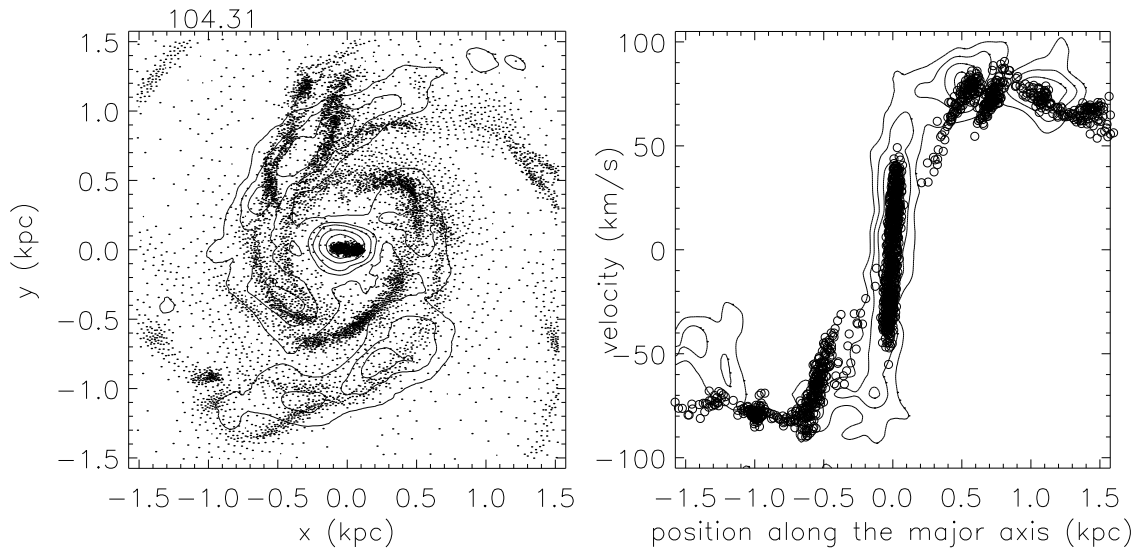


FIG. 7.—Same as Fig. 5, but for model 40

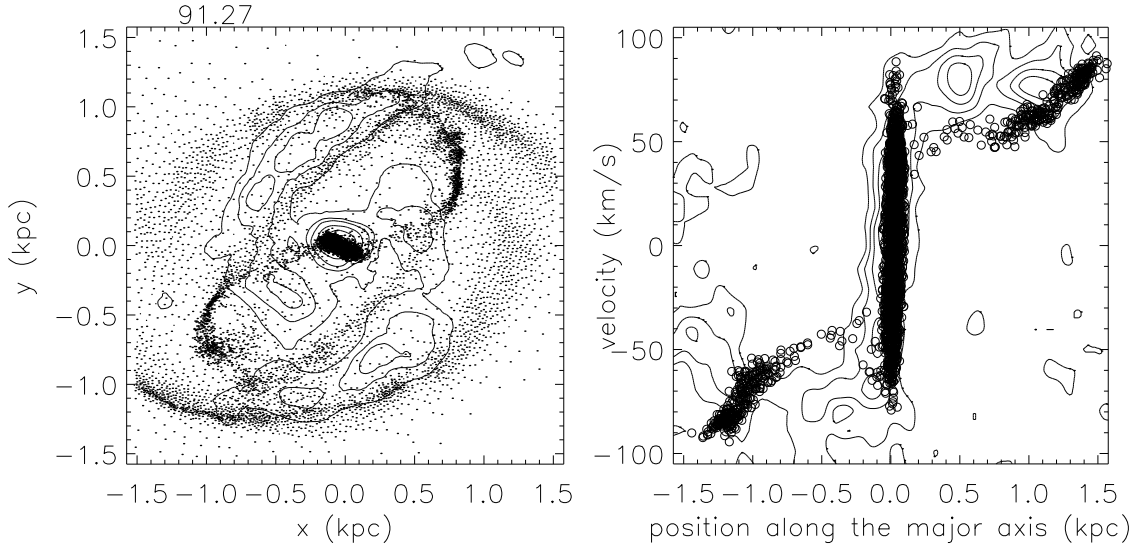


FIG. 8.—Same as Fig. 5, but for an NIR model, in which the pattern speed and the gas mass is the same as those in the best-fit analytical model (model 31) and $M/L_K = 0.4(M/L_K)_\odot$ is assumed.

observations has been found despite the fact that several tens of models with parameters near the best-fit values have been tested. The ranges of the parameters we have tested are $10 \leq \Omega_p \leq 160 \text{ km s}^{-1} \text{ kpc}^{-1}$, $0.1 \leq M_g \leq 2.0 \times 10^9 M_\odot$, $0.1 \leq \alpha \leq 4.0$, $1.0 \leq R_g \leq 2.5 \text{ kpc}$, where R_g is the initial radius of the gas disk. We have also added the extended disk component with various effective radii and masses into the NIR models, but the observations were not reproduced.

Thus, the results suggest that the assumption of the constant M/L_K , or the assumption of a single bar, or both, must be wrong. The assumption of a single bar is discussed in § 4.1. Here we derive a two-dimensional map of M/L_K assuming that the best-fit analytical model is the true potential of NGC 4321. We can derive the surface density distribution

$$\Sigma(R, \phi) = \int_{-\infty}^{\infty} \rho(R, \phi, z) dz, \quad (11)$$

using the Poisson equation

$$4\pi G \rho(R, \phi, z) = \frac{1}{R} \frac{d}{dR} \left(R \frac{d\Phi}{dR} \right) + \frac{1}{R^2} \frac{d^2\Phi}{d\phi^2} + \frac{d^2\Phi}{dz^2}, \quad (12)$$

where we use

$$\Phi \equiv \Phi(R, \phi, z) = \frac{c^2/a}{(R^2 + z^2 + a^2)^{1/2}} \times \left[1 + \frac{\epsilon_0 a R^2 \cos 2\phi}{(R^2 + z^2 + a^2)^{3/2}} \right]. \quad (13)$$

The three-dimensional potential (eq. [13]) is a simple extension of the two-dimensional bar model (eqs. [2] and [4]). It represents a three-dimensional bar with a smooth density profile. Hence, the surface density (eq. [11]) is

$$\Sigma(R, \phi) = \frac{3C\pi\epsilon_0 a(R^2 + 6a^2) \cos(2\phi)}{2(R^2 + a^2)^{7/2}} + \frac{4Ca^2}{(R^2 + a^2)^2}, \quad (14)$$

where $C \equiv v_{\max}^2(27/4)^{1/2}/(4\pi G)$. $\Sigma(R, \phi)$ is plotted for the best-fit model ($a = 300 \text{ pc}$ and $\epsilon_0 = 0.07$) in Figure 9. It is

clear that the mass distribution is rounder than the bar observed in the near-infrared light (Knapen et al. 1995b; Paper I).

Figure 10 (Plate 9) shows the M/L_K distribution derived from equation (14) and the K' -band image used for the NIR model. Here a disk potential ($a = 10 \text{ kpc}$ and $v_{\max} = 200 \text{ km s}^{-1}$) is taken into account. The surface density distribution is convolved with the Gaussian profile whose FWHM is the same as that of the observations, $2''.5$. It is clear that the M/L_K is not constant. The mass-to-luminosity ratio (1) becomes larger toward the center ($0.2 < R < 1.0 \text{ kpc}$), (2) shows the smallest value ($\alpha \sim 0.2$) at both ends of the nuclear bar, and (3) is smaller ($\alpha \sim 0.6$) at the center than in the circumnuclear regions ($R < 0.2 \text{ kpc}$). The last feature

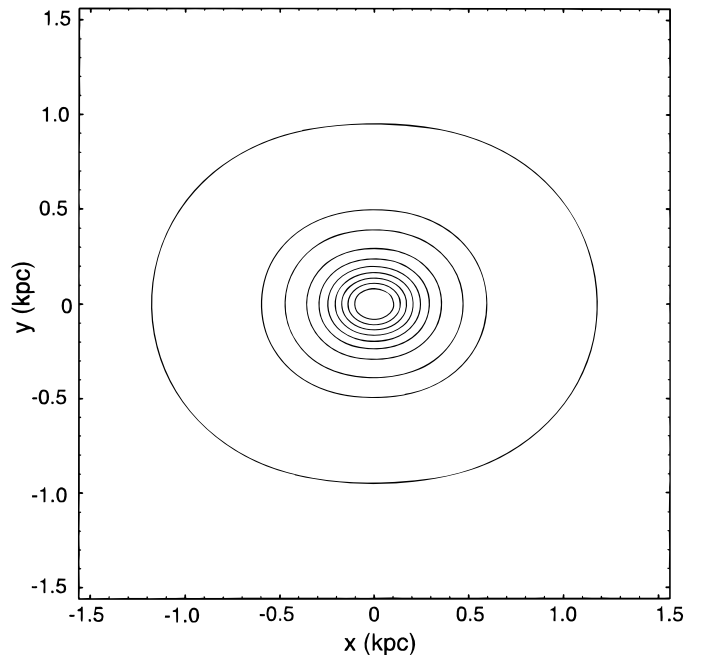


FIG. 9.—Surface density distribution in a face-on view (eq. [11]) with $a = 300 \text{ pc}$ and $v_{\max} = 180 \text{ km s}^{-1}$. Contour levels are $(0.1, 1, 2, 4, 6, 8, 10, 12, 14, 16) \times 10^3 M_\odot \text{ pc}^{-2}$.

might not be real because the size of the region is comparable to the resolution of the observations.

4. DISCUSSION

4.1. Bar Pattern Speed

The NIR observations show that there is a large bar structure ($R \sim 60'' \sim 5$ kpc) outside the inner bar ($R \sim 16'' = 1.3$ kpc) (Pierce 1986; Knapen et al. 1995a; Shaw et al. 1995; Paper I). Two descriptions of the relation between the two bars are possible: they form either a single bar or nested bars.

Since the position angles of these bars are nearly equal, Knapen et al. (1995a) concluded that only one stellar bar of $R = 60''$ exists in NGC 4321. They investigated gaseous evolution in an NGC 4321-like N -body bar ($R \sim 4$ kpc) and found that two-armed spirals similar to the CO observations are formed when the pattern speed of the N -body bar is ~ 2.6 in their unit ($\sim 68 \text{ km s}^{-1} \text{ kpc}^{-1}$). This is consistent with the pattern speed of our best-fit model ($65 \text{ km s}^{-1} \text{ pc}^{-1}$). We suppose therefore that the mass distribution in the inner region ($R < 2$ kpc) of the N -body bar is similar to that of our best-fit model. Knapen et al. (1995a) also showed that the offset straight shocks at the leading side of the outer bar are formed. This structure is similar to the BIMA observations, which revealed a straight ridge of molecular gas at the leading side of the outer bar (Rand 1995). Therefore, the whole molecular gas structure accompanied by the two bars could be formed even if NGC 4321 is a single-bar system (i.e., the nuclear bar and the outer bar rotate with the same pattern speed). In other words, the inner region of the single bar contributes to form the nuclear peak and the trailing spirals, and the straight shocks are formed owing to the outer region of the single bar. This kind of gaseous structure has been also observed in numerical simulations using a homogeneous bar plus a bulge component (e.g., Englmaier & Gerhard 1997). In such bar model, the composite mass distribution in the bulge region is also barlike, but its distortion is weaker than that in the outer region. The numerical simulations show that two-armed spirals are formed around the bulge radius for an appropriate pattern speed of the bar, because this is a turnover radius due to the bulge component, and thus the outer ILR is formed around the bulge radius.

Another possibility is that the two bars rotate with different pattern speeds. Observations of double-barred galaxies show that there is no preferred angle between the two bars (Buta & Crocker 1993; Friedli & Martinet 1993; Shaw et al. 1995). If this implies that the two bars rotate with different pattern speeds in double barred galaxies, NGC 4321 could be one of these now showing almost parallel configuration of the bars by chance. There have been two suggestions for the pattern speeds of the double barred galaxies. The first is that the inner-to-outer bar pattern speed ratio is about 3 (Friedli & Martinet 1993), and the other is that the pattern speeds are determined so that the ILR of the outer bar coincides with the CR (corotation resonance) of the nuclear bar (Friedli 1996 and references therein). The former is the case in NGC 4321 if the pattern speed of the inner bar is $65 \text{ km s}^{-1} \text{ pc}^{-1}$, as suggested in the present paper and the pattern speed of the outer bar is $\sim 20 \text{ km s}^{-1} \text{ pc}^{-1}$, as suggested by Sempere et al. (1995). The latter possibility was not examined in this paper. In either case, the gas orbits must be highly complicated under the influence of the two

periodic perturbations. It is not clear at this point whether the observed molecular gas structure is reproduced in the double-barred system. In order to investigate the possibility of double bars, further numerical simulations and further observational studies are necessary.

4.2. Mass and M/L Distribution

The two-dimensional map of the mass-to-NIR luminosity ratio (Fig. 10) shows that M/L_K is mostly between $0.2(M/L)_\odot$ and $0.8(M/L)_\odot$ in the regions inside $R \sim 1.0$. This is consistent with the estimates in the literature for the central regions of spiral galaxies. (e.g., $M/L_K = 0.45 \pm 0.15(M/L)_\odot$: Bottema 1992; and $0.35 \pm 1.4(M/L)_\odot$: Devereux, Becklin, & Scoville 1987). The M/L_K map also shows a ratio in excess of this range at the central region ($R < 300\text{--}700$ pc) and a minimum of the ratio at the ends of the nuclear bar. The latter is probably due to the hot dusts and/or red supergiants in the star-forming region at the bar ends (Knapen et al. 1995a). There are a number of star-forming regions around the nuclear bar to affect its shape and size in NIR, from which the gravitational potential is estimated in the NIR model. Consequently, it is reasonable that the NIR models, in which the constant M/L_K is assumed, do not match the observations (§ 3.2).

In addition to the star-forming regions at the bar ends, there are three other H II regions: two just inside the spiral arms and one at the center (Cepa & Beckman 1990, see also Fig. 9 in Paper I). The star-forming regions near the spiral arms, however, do not affect the M/L_K distribution in Figure 10. This can be understood if the star-forming regions at the arms have an age different than that of the H II regions at the bar ends. It is because the M/L_K ratio of a star-forming region changes widely in its early age; e.g., for a single age stellar population with the same metallicity, M/L_K varies by a factor of 10 in the first 10^8 yr (Kodama 1997). The age difference of $\sim 10^7$ yr between star-forming regions seems possible because the whole gas structure evolves in a similar timescale (cf. Fig. 2).

4.3. Gas Mass

In § 3.1.3, we have determined the total gas mass in the central region of NGC 4321 to be $\sim 1.0\text{--}1.3 \times 10^9 (T_g/10^4 \text{ K})^{1/2} M_\odot$. The temperature dependence originates from the local gravitational instability condition in a gas disk. In a very massive disk, the gravitational instability grows nonlinearly, and the disk turns into a clumpy system before the resonant structure, such as the spirals at the ILR's, evolves. In a less massive disk, however, the spiral arms are gravitationally stable, and no clumps are formed on the arms. The gaseous system with the isothermal temperature T_g in our simulations corresponds to a system with the sound velocity $v_s \sim 10(T_g/10^4 \text{ K})^{1/2} \text{ km s}^{-1}$, such as a molecular cloud system with the velocity dispersion $\sigma \sim v_s$. Our results imply that the total gas mass is $\sim 0.5\text{--}2.6 \times 10^9 M_\odot$ if the velocity dispersion is in the range of $5\text{--}20 \text{ km s}^{-1}$, as measured in other spiral galaxies (e.g., Sakamoto 1996). On the other hand, the H_2 mass estimated from the luminosity of the ^{12}CO ($J = 1\text{--}0$) is $2.2 \times 10^9 M_\odot$ (Paper I), assuming the CO-to- H_2 conversion factor determined from giant molecular clouds in the Galactic disk (Sanders, Solomon, & Scoville 1984). It is remarkable that our numerical estimate for gas mass agrees with that from CO luminosity within a factor of 2.

In our numerical approach, if we know the gaseous kinematic temperature or the velocity dispersion, the mass of gas in galaxies can be evaluated more precisely. We find that $T_g = 10^4$ K is better for reproduction of the observations than $T_g = 4 \times 10^4$ K, with respect to gaseous morphology and two quantities: the line-of-sight velocity dispersion at the central core and the ratio of the surface density at the central peak and at the most dense clump on the arms. Thus, the total gas mass would be $\sim 1.0 \times 10^9 M_\odot$ rather than $\sim 2.0 \times 10^9 M_\odot$. If this is the case, the CO-to-H₂ conversion factor in the central regions of NGC 4321 should be a factor of 2 smaller than the Galactic disk value, consistent with the recent studies of the conversion factor (e.g., Nakai & Kuno 1995; Arimoto, Sofue, & Tsujimoto 1996; see also Rand 1995 for NGC 4321).

5. CONCLUSIONS

We have compared the CO interferometry observations with the two-dimensional hydrodynamic simulations of gas disks in gravitational potentials that suitably match the nuclear region of NGC 4321. For constructing the gravitational potential, we have used both a K' -band image with a constant M/L_K and an analytical description of a bar, in which M/L_K is not constant. The hydrodynamic simulations were performed using the SPH method taking into account the self-gravity of the gas. We have quantitatively confirmed the conclusion of Paper I: the inner Lindblad resonances can cause the molecular gas structure (two trailing spirals and a dense central core). Assuming that the nuclear bar ($R \sim 16'' \sim 1.3$ kpc) observed in the near-infrared contributes mainly to the gaseous dynamics in the nuclear bar region, the following points are revealed:

1. The best set of analytical bar model parameters for reproduction of the observations was determined. The best

pattern speed of the inner bar is $65 \text{ km s}^{-1} \text{ kpc}^{-1}$, which is consistent with the value estimated by Knapen et al. (1995a) but is about 3 times larger than that of the outer bar suggested by Sempere et al. (1995).

2. The total mass of gas in the region of $R < 1.5$ kpc was estimated in a dynamical way to be $\sim 1.0\text{--}1.3 \times 10^9 (T_g/10^4 \text{ K})^{1/2} M_\odot$, where T_g is the gas kinematic temperature. This estimate is independent of that from CO luminosity, but agrees with it within a factor of 2.

3. The observed morphology of the molecular gas is a short-lived and recurrent structure. The spiral structure lasts for about 10^7 yr at the observed position, and it is produced again after about 10^8 yr.

4. The models with a constant mass-to-luminosity ratio (M/L_K) and a single pattern speed do not reproduce the observations.

5. A two-dimensional map of M/L_K was derived from the potential of the best fit model and the K' -band image. The M/L_K ranges from 0.2 to 1.2 (M/L_\odot) at $R < 1.5$ kpc. The M/L_K is not constant but is strongly affected by star formation, as suggested by Knapen (1995b). Thus, the K' luminosity is not an accurate tracer of mass distribution in the central region of NGC 4321.

Numerical computations were carried out on VPP500 in RIKEN and on VY/4R and VX/4R at the Astronomical Data Analysis Center of the National Astronomical Observatory, Japan. We thank T. Ebisuzaki and staff of computational science laboratory in RIKEN for their support. We are also grateful to I. Shlosman, J. Knapen, C. Yuan, A. Habe, and Y. Sofue for their valuable comments. This work was supported in part by NAO. K. S. and T. M. were supported by the Grant-in-Aid for JSPS Fellows by the Ministry of Education, Science, and Culture. H. K. was supported by the Hokscitec Foundation.

REFERENCES

- Arimoto, N., Sofue, Y., & Tsujimoto, T. 1996, PASJ, 48, 275
 Bottema, R. 1992, A&A, 257, 69
 Buta, R., & Crocker, D. 1993, AJ, 105, 1344
 Cepa, J., & Beckman, J. E. 1990, A&AS, 83, 211
 Devereux, N. A., Becklin, E. E., & Scoville, N. 1987, ApJ, 312, 529
 Englmaier, P., & Gerhard, O. E. 1997, MNRAS, 287, 57
 Friedli, D., & Martinet, L. 1993, A&A, 277, 27
 Friedli, D. 1996, in Barred Galaxies, ed. R. Buta, D. A. Crocker, & B. G. Elmegreen (San Francisco: ASP), 378
 Hockney, R. W., & Eastwood, J. W. 1981, Computer Simulation Using Particles (New York: McGraw Hill)
 Knapen, J. H., Beckman, J. E., Heller, C. H., Shlosman, I., & de Jong R. S. 1995a, ApJ, 454, 623
 Knapen, J. H., Beckman, J. E., Shlosman, I., Peletier, R. F., Heller, C. H., & de Jong, R. S. 1995b, ApJ, 443, L73
 Kodama, T. 1997, Ph.D. thesis, Univ. Chicago
 Nakai, N., & Kuno, N. 1995, PASJ, 47, 761
 Pierce, M. J. 1986, AJ, 92, 285
 Rand, R. J. 1995, AJ, 109, 2444
 Sakamoto, K. 1996, ApJ, 471, 173
 Sakamoto, K., Okumura, S., Minezaki, T., Kobayash, Y., & Wada, K. 1995, AJ, 110, 2075 (Paper I)
 Sanders, R. H. 1977, ApJ, 217, 916
 Sanders, D. B., Solomon, P. M., & Scoville, N. Z. 1984, ApJ, 276, 182
 Shaw, M., Axon, D., Probst, R., & Gatley, I. 1995, MNRAS, 274, 369
 Sempere, M. J., Garcia-Burillo, S., Combes, F., & Knapen, J. H. 1995, A&A, 296, 45
 Toomre, A. 1963, ApJ, 138, 385
 Wada, K., & Habe, A. 1992, MNRAS, 258, 82
 ———. 1995, MNRAS, 277, 433

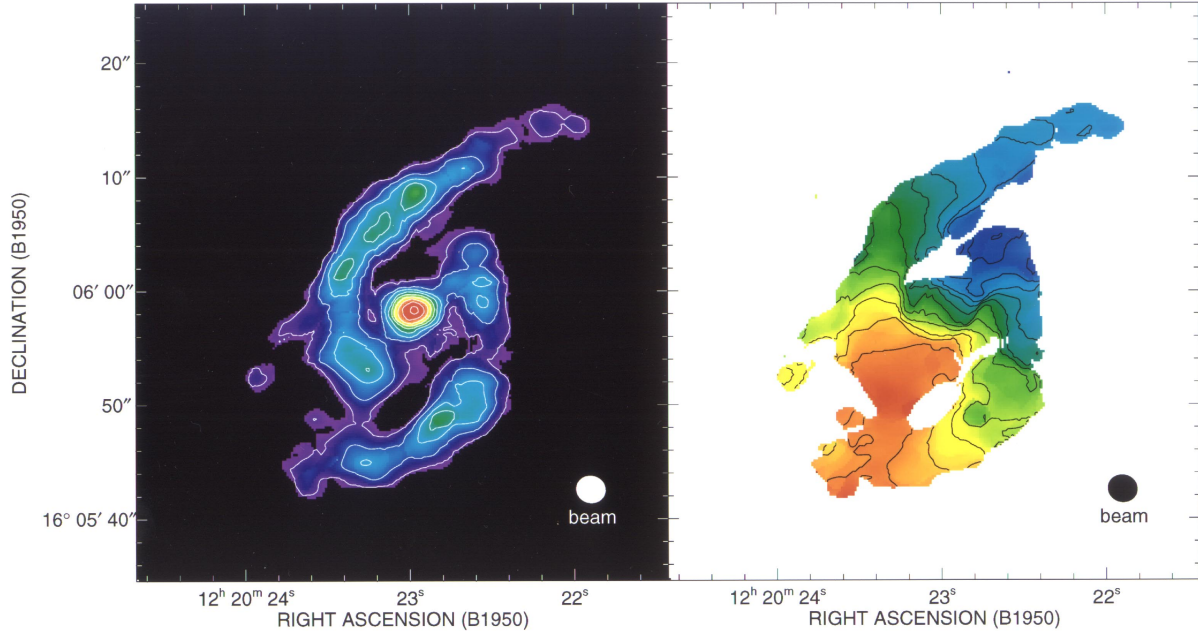


FIG. 1.—*Left*: Integrated intensity map of the CO $J = 1-0$ emission in the central region of NGC 4321 (see Paper I). Contours are 2, 4, 6, ..., 16, 18 times $1.5 \text{ Jy beam}^{-1} \text{ km s}^{-1}$. *Right*: Intensity-weighted isovelocity map of the CO $J = 1-0$ emission. Contours are in steps of 15 km s^{-1} from -100 km s^{-1} . Band center is 1574 km s^{-1} (LSR).

WADA, SAKAMOTO, & MINEZAKI (see 494, 238)

PLATE 7

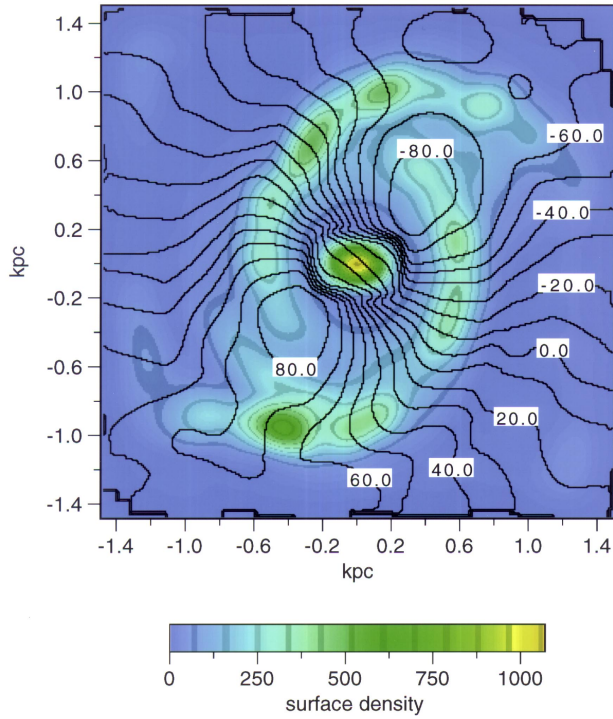


FIG. 4

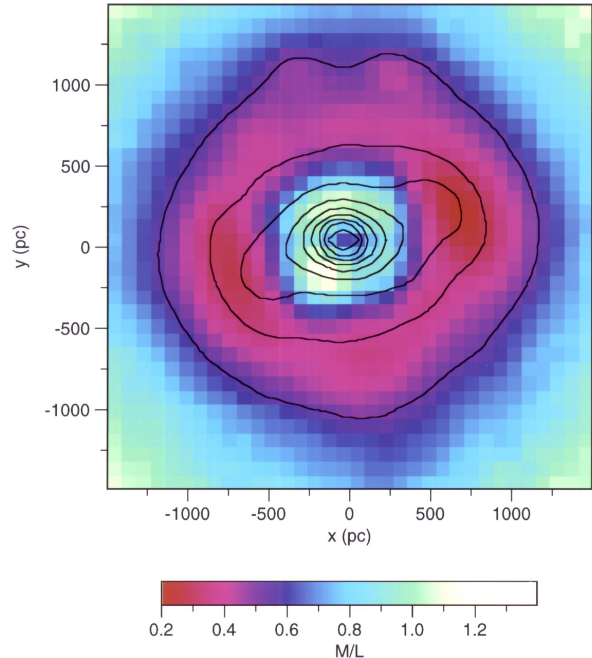


FIG. 10

FIG. 4.—Density map in a face-on view (*bottom*) and an isovelocity contour map (*top*) of $T = 101.67 \text{ Myr}$ of the snapshot ($T = 101.67$) in model 31. The original data obtained by the SPH simulation is convolved in the Gaussian beam of 200 pc in FWHM. Units of the surface density and the velocity are $M_{\odot}/M_{\odot} \text{ pc}^{-2}$ and km s^{-1} .

WADA, SAKAMOTO, & MINEZAKI (see 494, 241)

FIG. 10.—Mass-to-luminosity ratio (M/L_K) map in the face-on view derived the mass distribution for the best-fit analytical bar model (eq. [11]) with an extended disk potential and K' -band image (see Paper I). The color represents M/L_K in units of $(M/L)_{\odot}$.

WADA, SAKAMOTO, & MINEZAKI (see 494, 244)

PLATE 8/9